Available online at www.sciencedirect.com
SCIENCE DIRECT®
Earth and Planetary Science Letters 244 (2006) 323–335
EPSL
www.elsevier.com/locate/epsl

Subglacial geology in Coats Land, East Antarctica, revealed by airborne magnetics and radar sounding

T. Shepherd [a], J.L. Bamber [a,*], F. Ferraccioli [b]

[a] *Bristol Glaciology Centre, School of Geographical Sciences, University of Bristol, BS8 1SS, UK*
[b] *British Antarctic Survey, Madingley Road, Cambridge, UK*

Received 7 September 2005; received in revised form 25 January 2006; accepted 30 January 2006
Available online 9 March 2006
Editor: S. King

Abstract

During the austral summer of 2001/02 five thousand line kilometres of airborne radio echo sounding and aeromagnetic data were collected in the region of three tributaries of Slessor Glacier, East Antarctica, which drains into the Filchner Ice Shelf. Basal topography and roughness estimates were obtained from the echo sounding data, which have been combined, here, with the subglacial geological units inferred from an analysis of the aeromagnetic data. This analysis included Euler and Werner deconvolution to determine the location and depth of sills, dykes and faults. In addition, we high-pass filtered the magnetic anomaly profiles to obtain information about the near surface subglacial geology. This revealed a prominent area of low magnetic susceptibility lying in a deep topographic basin underneath the northern tributary of Slessor Glacier. Forward and inverse magnetic models indicate that this area is likely underlain by a 3 km thick sedimentary basin. Ice flow modelling suggests that this sedimentary basin influences the ice dynamics in the tributary. These results have important implications for understanding the dynamics of this and other East Antarctic flow features that may be underlain by a weak sedimentary bed.

Keywords: Slessor Glacier; subglacial sediments; aeromagnetics; East Antarctica; radio echo sounding

1. Introduction

The East Antarctic Ice Sheet (EAIS) contains about 80% of the land ice on the planet. Understanding the mechanisms that control the flow of the ice is, therefore, central to our ability to understand and model the past, present and future behaviour of the ice sheet. The motion of ice in Antarctica is the result of three mechanical processes: internal deformation of the ice (also known as creep), sliding of the ice over bedrock and shear of a layer of deformable sediment at the ice/bed interface. One or more of these processes may be present at any particular place across the ice sheet. The latter two processes, however, require the presence of water at the bed and, in the case of the third process, a substantial layer of water-saturated sediment. So while internal deformation takes place everywhere where there is horizontal ice motion, basal sliding and deformable sediments have additional requirements that are not met everywhere. When present, basal motion can, however, be responsible for 90% or more of the total ice velocity. As a consequence, understanding the factors that influence basal motion is crucial to our understanding of ice sheet dynamics and our ability to adequately model ice flow.

* Corresponding author.
E-mail address: J.Bamber@bristol.ac.uk (J.L. Bamber).

0012-821X/$ - see front matter © 2006 Elsevier B.V. All rights reserved.
doi:10.1016/j.epsl.2006.01.068

Most of the EAIS is grounded on bedrock that is above sea level. For the West Antarctic Ice Sheet (WAIS), the converse is the case and it is, consequently, often termed a marine ice sheet. As a consequence, much of the WAIS has the potential to be underlain by marine sedimentary deposits and these (where identified) have been linked with the existence and behaviour of active ice streams and glaciers [1–3]. Unlike the WAIS, very little is known about the subglacial geology underlying areas of enhanced flow beneath the EAIS. Partly to redress this gap in our knowledge, an airborne geophysical survey was undertaken in the austral summer of 2001/02 in the vicinity of two enhanced flow features in the Bailey/Slessor region of East Antarctica (Fig. 1). The key aerogeophysical instruments onboard were a radio echo sounding (RES) system, for measuring ice thickness and basal characteristics [2], and a magnetometer for determining total magnetic intensity (TMI). The RES data were processed to provide information on bed topography, basal roughness and returned power strength. The results of this have been presented elsewhere [2] and are not discussed in detail here. In this paper we present the results of the aeromagnetic survey and the implications, which they,

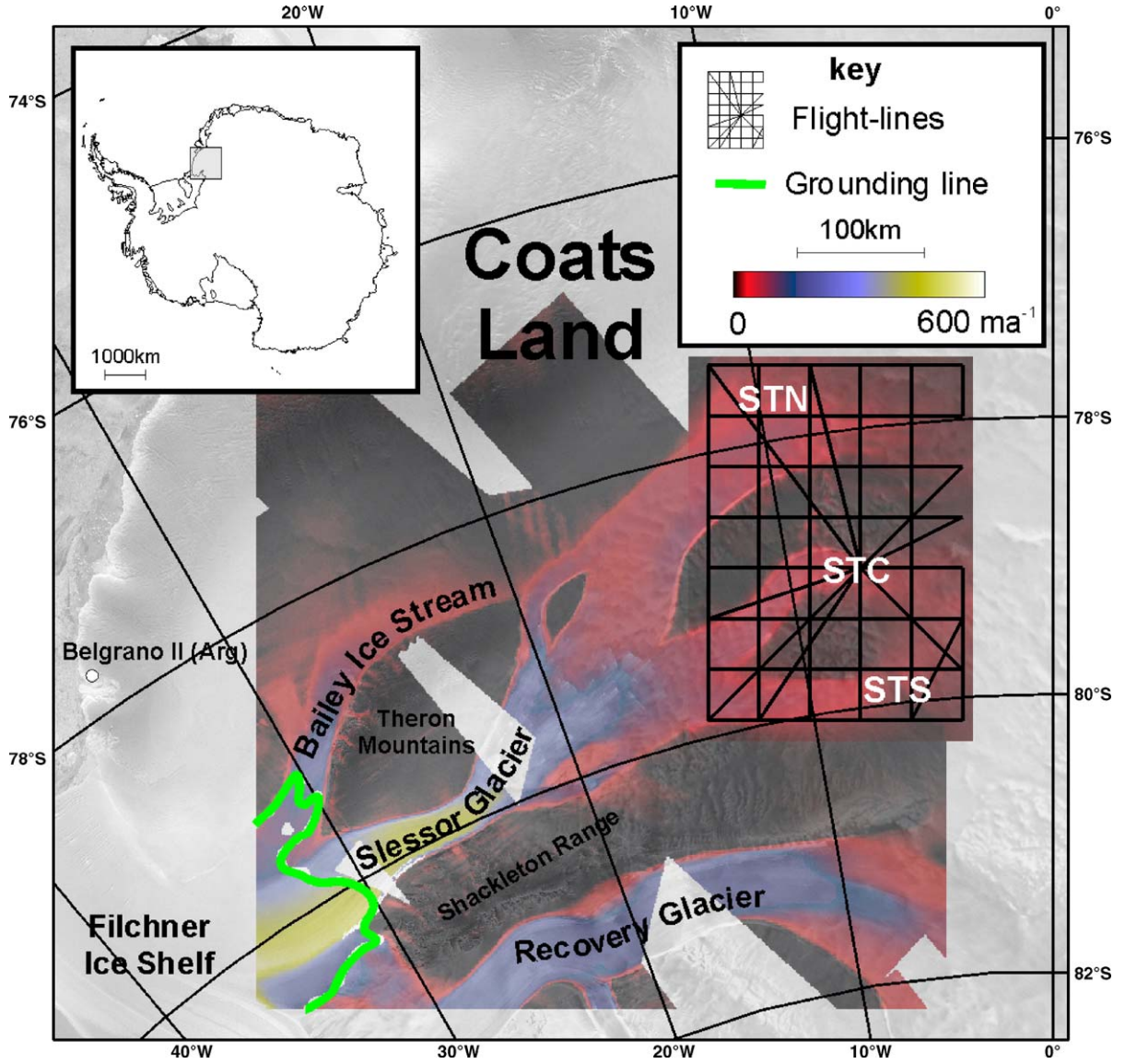

Fig. 1. Regional map showing the survey flight lines and ice motion over the northern, central and southern Slessor Glacier tributaries, labelled STN, STC and STS, respectively. The background is taken from the RAMP synthetic aperture radar mosaic [36]. The inset shows the location of the study area (shaded box) in Antarctica.

in conjunction with the RES results and ice dynamics modelling, have for possible geological controls on enhanced flow in East Antarctica.

2. Data sets

2.1. Airborne geophysical survey

Data were collected during five 1000 km survey flights covering an area of 200×280 km, about a base/re-fuelling camp located at 78° 58.60′ S, 007° 24.97′ W (Fig. 1). The survey was flown using a DeHavilland Twin Otter aircraft of the British Antarctic Survey. A near-constant terrain clearance of 85 m was maintained from the ice surface, monitored by the aircraft's radar altimeter system. Longitudes and latitudes on the WGS84 ellipsoid were recorded for each measurement by a GPS receiver and later projected into polar stereographic co-ordinates. Altitudes for all measurements were recorded by the GPS and differentially corrected with reference to a second receiver at the base station.

2.2. Aeromagnetic data

The scalar quantity of TMI was measured by a caesium magnetometer flown in fixed-wing configuration. Point measurements were taken at 100 ms intervals (10 Hz) which, with a near-constant aircraft speed of ~60 ms^{-1}, gives along-track profile data every ~6 m. The sensitivity of the Cs-2 sensor was 0.001 nanotesla (nT). The across-track spacing between flight lines was 40 km. In addition aeromagnetic data were collected along ferry-lines (Fig. 1). This provides a relatively coarse mesh of primary data for an aeromagnetic survey, reflecting a compromise between the available flight time and the survey area. All data were low-pass filtered with a 5 data point smoothing window to remove artefacts of aircraft motion. Data were corrected for regional diurnal variations recorded by a proton-precession magnetic base station installed at the camp. The sampling rate was 30 s. The raw base station data were filtered with a 10 min low-pass filter. Flights were performed during relatively quiet magnetic periods, to ensure that the data were not corrupted by external magnetic field variations, which can be significant in polar regions. The geomagnetic reference field was calculated using the IGRF 2000 model coefficients, and subtracted from the base station corrected survey data to remove the effect of the core field. Finally, statistical levelling and microlevelling procedures were applied to reduce crossover errors [4].

2.3. Subglacial topography

Bedrock elevation was measured along the survey flights by the RES system. The British Antarctic Survey (BAS) airborne radar operated with chirped pulse modulation achieving deep ice penetration and an along-track spacing of ~25 m. Nonetheless, in some areas no bed echoes were obtained. We re-sampled RES data at an along-track spacing of 2 km, which served to smooth the raw data and give continuity where data were missing. A bed elevation model was produced at 5 km spacing, which was used to correct the TMI data, as described below, and to examine what topographic control existed on the location of the three tributaries of Slessor Glacier covered during the survey [2].

2.4. Ice dynamics and tributary location

Several additional data sets have been used to help elucidate the dynamic setting of the area. The most important of these are estimates of ice surface velocity derived from interferometric synthetic aperture radar (InSAR) techniques and balance velocities. The former were obtained from RADARSAT data [5,6]. The latter is an estimate of the velocity field based on the assumption that the ice sheet is in a state of balance and integrating snow accumulation along the path of ice motion. These balance velocities provide a good representation of the general pattern of flow [7]. They are, however, an approximation for the actual surface velocity field and were used only where no InSAR data were available (Fig. 1). They were adjusted to match the InSAR-derived velocities in an area of overlap between the two. Here, the combined velocity data set is used to indicate the location of areas of enhanced flow and, in particular, the location of the three Slessor tributaries labelled in Fig. 1.

In addition to InSAR data and balance velocities, we identified tributary locations in radar imagery from the RADARSAT Antarctic Mapping Project (RAMP). Shear margins of tributaries show up as distinct linear features where crevassing occurs near the ice surface. By overlaying flight lines onto RAMP data in a geographical information system (GIS) we located the intersections of flight lines with shear margins (Fig. 2b–d). These mark the boundary between tributaries and inter-tributary regions.

3. Methodology

The deeper tectonic setting was investigated by interpreting the magnetic anomaly map with the aid of

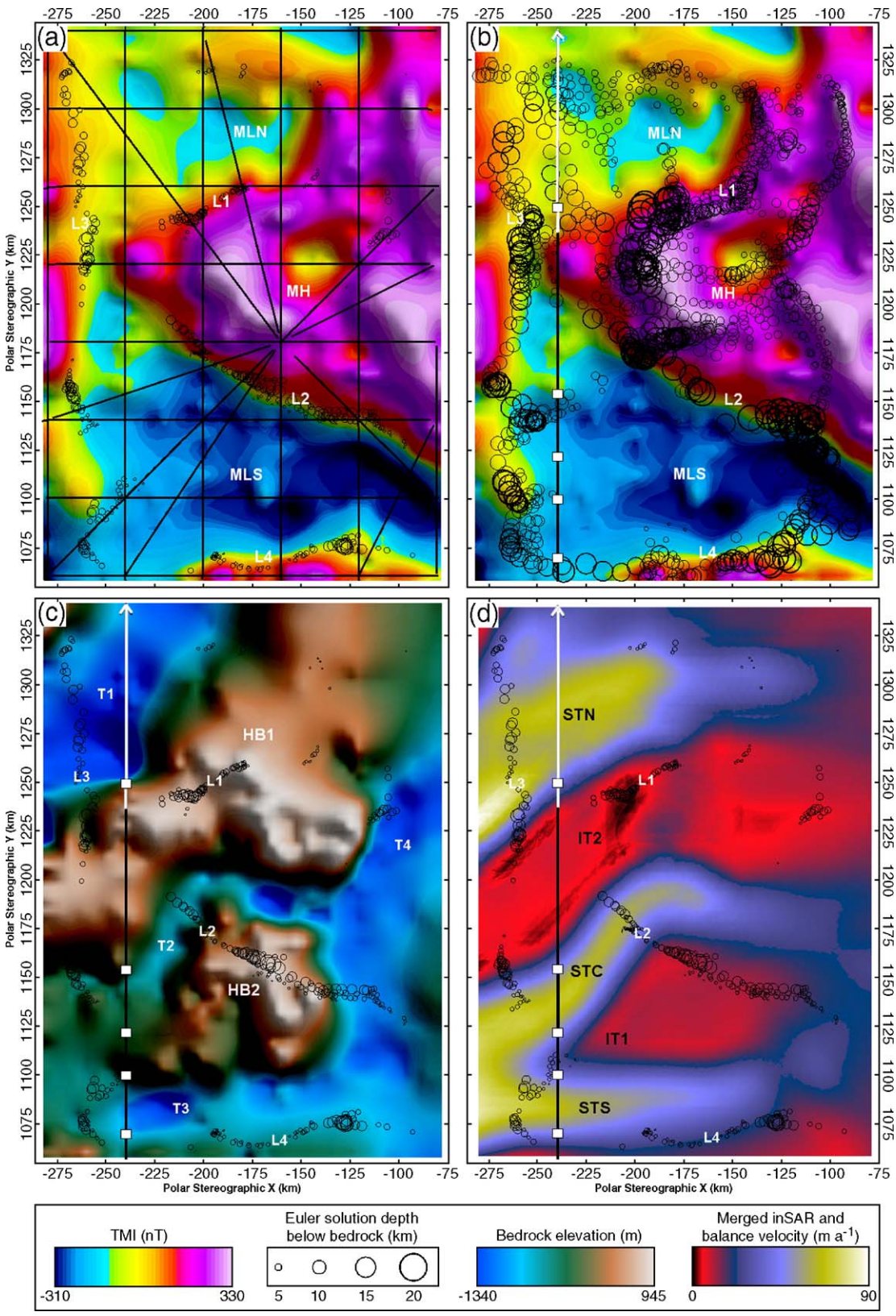
(a)
(b)
(c)
(d)
MLN
L1
L3
MH
L2
MLS
L4
T1
HB1
T4
T2
HB2
T3
STN
IT2
STC
IT1
STS
Polar Stereographic Y (km)
Polar Stereographic X (km)
-275 -250 -225 -200 -175 -150 -125 -100 -75
1325 1300 1275 1250 1225 1200 1175 1150 1125 1100 1075
TMI (nT)
-310 330
Euler solution depth below bedrock (km)
5 10 15 20
Bedrock elevation (m)
-1340 945
Merged inSAR and balance velocity (m a-1)
0 90

Euler deconvolution [8]. To focus on the surface bedrock properties (which are what are relevant to the ice dynamics) we then analysed TMI profiles, which contain the higher-frequency information necessary to investigate shallower magnetic properties.

TMI anomalies are governed by the source's magnetic susceptibility, along with the geometry and distance between source and measurement instrument [9,10]. It is the properties of the *surface* bedrock that are of particular glaciological significance. Notably, a near-zero susceptibility is characteristic of soft marine sediments, believed to have a key influence on basal deformation rates, as discussed earlier. Unlike basement rock, or sedimentary deposits from eroded bedrock, the low susceptibility of marine sediments means they acquire negligible induced magnetization and hence do not contribute to the observed TMI. Our approach here was to separate contributions to TMI from deep and shallow rock, and relate the latter to surface bedrock susceptibility. First we minimised the effect of the varying distance between the magnetometer on the aircraft and bedrock (with two-dimensional draping using a clearance of 2 km, [11]) and then removed the influence of deep magnetic sources (using residual anomalies, [12]). The results were compared with those from inverse modelling using Werner deconvolution [13], which provides an estimate of the depths and susceptibilities of the sources. Finally we produced a simple forward model [10] to further constrain the geometries of the magnetic anomaly sources in the area of the northern tributary of the Slessor Glacier.

3.1. 3D Euler deconvolution

The gridded TMI shown in Fig. 2a and b improves our understanding of the deep geological setting and also allows 3D imaging of geological features by Euler deconvolution. First, a minimum curvature surface fit was used to interpolate profile data on a grid with 5×5 km cell spacing. Euler's homogeneity relation then leads to the location of a magnetic source in 3 dimensions from its field observed at a given point [8].

The source being located is approximated to either a line of magnetic poles or a 'point pole'. These are used as idealised models for geological 'contacts' or the edges of 'dykes' and 'sills'. A contact is essentially a boundary between large expanses of different rock units. Dykes are near-vertical intrusions narrow in one horizontal direction and sills are tabular bodies. Dykes and sills are indistinguishable by Euler deconvolution as their ideal fields have a common degree of homogeneity. The degree of homogeneity is defined as the integer n in the general form of Euler's relation: $\boldsymbol{r} \cdot \nabla T = -nT$, where $\boldsymbol{r}$ is the position vector of the magnetic source giving anomalous field T. The integer n is known as the structural index (SI) and provides a means of differentiation between a contact and a dyke/sill. We use values of 0 to locate contacts, or major faults, and 1 to locate dykes, sills or faults with limited throw (Fig. 2a and b).

The method is invariant to the dip or strike of a feature, and by scanning the whole grid, faults are located as linear clusters of solutions. Deconvolution windows of 10×10 grid cells (equivalent to 50×50 km) proved necessary to resolve magnetic lineaments in our study. This limited the method, however, to resolving the location of deeper sources only. As a rule, Euler solutions are not reliable at depths of less than 1 grid cell dimension (5 km) below observation [8]. After draping the data (see below) this corresponds to a minimum depth of 3 km below bedrock.

3.2. Residual anomalies

Longer wavelength TMI features are generally caused by deeper sources while magnetic rocks approaching the bedrock surface give rise to shorter wavelength features, superimposed onto regional-scale anomalies [10]. Residual profiles are produced when some signal is subtracted from the TMI. Contributions from deeper geology are commonly removed to enhance TMI signatures arising from shallower anomaly sources. Here we obtained residual profiles by 'upward continuation' of the TMI data (e.g. [14,15]). This was done by subtracting upward-continued data (1 km) from the draped TMI data (Fig. 3d). Another method is to define the regional anomaly by some wavelength limit [16], which is achieved by subtracting smoothed TMI data from *a low-pass filtered version* (Fig. 3e). The wavelength cut-off used in the low-pass filter is the maximum wavelength present in the residual. The limiting

Fig. 2. (a) Draped aeromagnetic anomaly map at 2 km above bedrock. Shading with 45° inclination and declination illumination directions is applied to enhance trends. 3D Euler deconvolution solutions, as obtained for structural index SI = 0, are overlain as circles with diameters proportional to their depth. Note the main magnetic lineaments L1–L4, the magnetic high MH, and the flanking lows MLN and MLS. (b) Same as panel (a), but with Euler deconvolution solutions for SI = 1; (c) shaded relief subglacial topography map from RES data (45° inclination and declination). Note troughs T1–T4 and highland blocks HB1 and HB2; (d) combined inSAR and balance velocities over the Slessor Glacier tributaries STN, STC and STS and inter-tributary regions IT1 and IT2. The location of tie line T1020 is marked by the solid line in panels b–d, along with its direction (arrow). White boxes denote its intersection with RAMP shear margins. Solid white line shows the location of the magnetic modelling section.

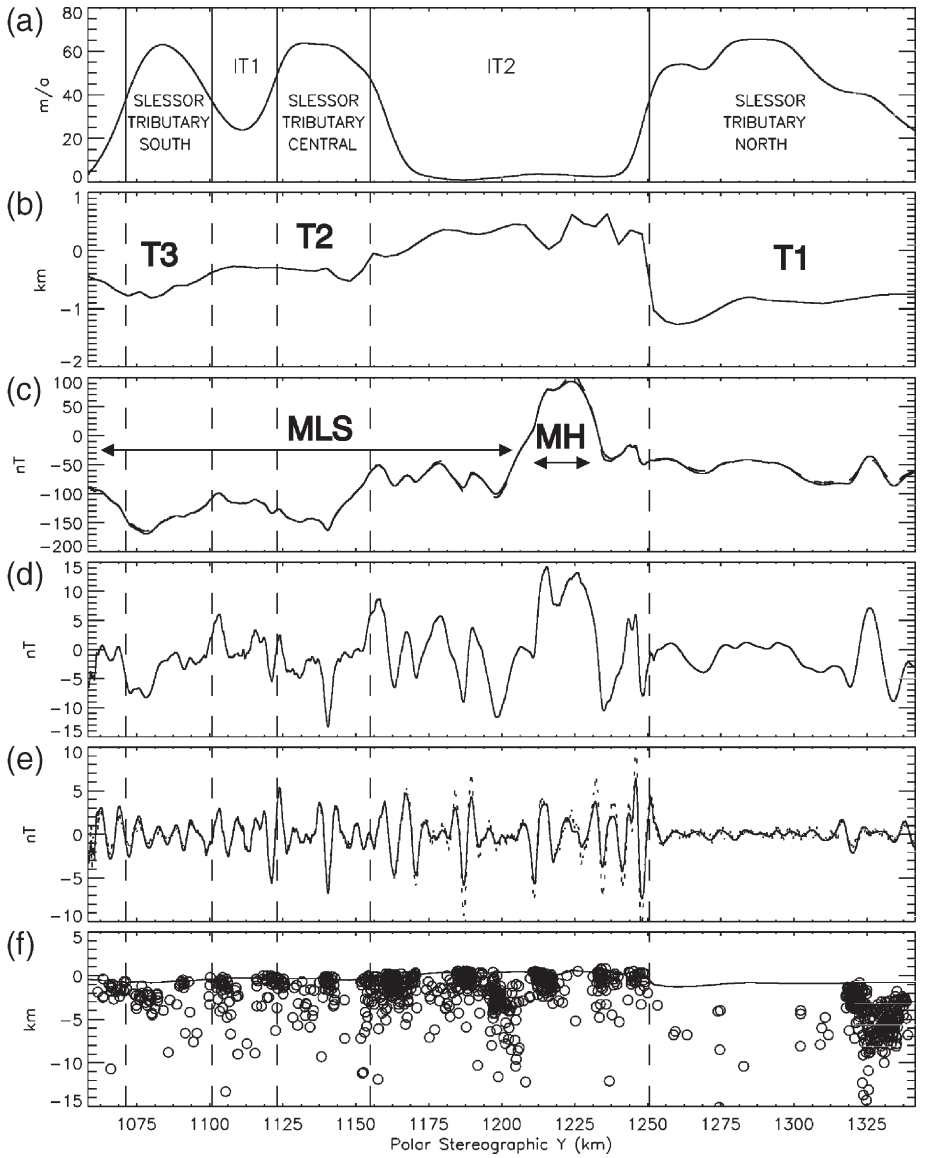

Fig. 3. Profile data views along tie line T1020. (a) Combined InSAR and balance velocities. Solid vertical lines denote the locations of RAMP-derived shear margins separating tributaries from inter-tributary regions. These margins are projected as dashed lines in the other five panels; (b) bedrock elevation from RES data; (c) draped (solid) and original (dashed) TMI profiles, which are almost identical along this profile; (d) residual anomalies produced by subtracting data upward-continued to 1 km from the draped TMI data. (e) Residual profile produced by subtracting low-pass filtered data from the draped (solid line) and original (dotted line) TMI data. (f) Depth estimates for shallow magnetic sources (circles) from Werner deconvolution, applied to the residual by upward continuation. Solid line shows the bedrock elevation profile.

wavelength is commonly chosen by inspection of the radially averaged power spectrum (RAPS) of TMI data [17]. The low-pass filter we adopted was assigned a cut-off of 1500 data points, corresponding to a wavelength of ~9 km. This places an upper bound on the depth range under investigation, which is loosely quantifiable. By analysing the RAPS of all original TMI data, we ascertained that a filter wavelength of 9 km corresponds to a depth of approximately 2–4 km below observation altitude. For our draped data, this corresponds to a ~2 km thick layer with its top placed at the surface of subglacial bedrock. For such an under-constrained problem, this relationship between wavelength cut-off and depth range cannot be considered definitive. However, a further constraint on the depth of the corresponding magnetic sources is given by Werner deconvolution, as discussed next. The *residual by low-pass filtering* has both positive and negative values centred around zero,

which makes it easy to identify the along-profile variation in high-frequency patterns (Fig. 3e) from the *amplitude of residual anomalies* (AOR).

3.3. Werner deconvolution

Two-dimensional Werner deconvolution is used to determine the depth to magnetic sources, from anomalies along a profile [13]. The method analyses a TMI profile to locate sources, approximated to semi-infinite sheets of magnetic dipoles. The location given is that of the 'top' of this ideal sheet. A deconvolution window of several data points is shifted along the profile and at each position, solves simultaneous magnetic field equations by a nonlinear Marquardt least squares method [13]. By only accepting certain solutions, a distribution of source depths is built up along the profile. Acceptance is based upon two thresholds; first, the localised amplitude of the TMI within a window is given a minimum. This is characterised by the RMS residual after removal of the linear trend within a window. Second, an upper limit is given to the horizontal displacement of a solution from the window's position along the profile. As previously mentioned, we applied Werner deconvolution to the residual *by upward continuation*, in order to focus our analysis on shallow sources. We used an iterative routine to analyse the profile with windows of increasing width from 2 to 20 km. These widths are based upon visual inspection of features in the residual by upward continuation, and represent a wavelength range centred on the 9 km cut-off used to calculate the residual by low-pass filtering.

4. Results

4.1. Magnetic anomaly patterns and lineaments

The draped TMI map (Fig. 2a–b) reveals the marked contrast between the highly magnetic region labelled MH, and the flanking magnetic lows to the North and South, labelled MLN and MLS, respectively. MH is a predominantly positive, long wavelength feature. Superimposed onto this regional positive anomaly are relatively shorter wavelength anomalies of around 60–80 km wavelength, reaching peaks up to 300 nT. While MLN has mean values around −50 nT, MLS is distinctly more negative with mean values around −150 nT and a minimum of −300 nT. The latter also features more distinct high-frequency anomaly patterns.

The boundary between MH and MLN is marked by a sharp ENE–WSW oriented gradient. At $x=-240$ E, this sharp gradient turns to an approximately NE–SW trend. We define this magnetic gradient as L1. L1 is located by Euler deconvolution, wherein only the E–W linear segment is identified using SI=0 (Fig. 2a) corresponding to contacts or large-throw faults, whereas the whole curvilinear feature is clearly located in Fig. 2b using SI=1, corresponding to dyke/sill sources or faults with more limited throw. The boundary between MH and MLS is marked by a prominent WNW–ESE oriented gradient (L2). L2 is clearly located by Euler deconvolution using both structural indices 0 and 1 (Fig. 2a–b), with SI=1 giving deeper solutions. Two additional magnetic lineaments can be recognised by Euler deconvolution. L3 is oriented approximately in a N–S direction. It appears to be a discontinuous feature, and extends for over 250 km. L4 is oriented approximately E–W and provides a Southern boundary to MLS.

Within MLN, there are poorly clustered Euler solutions (SI=1) that fall within the depth range of 5–10 km (Fig. 2b). Notably, there is an apparent lack of similar solutions within MLS. This reflects the choice of the Euler deconvolution window (10×10 grid cells), which is unable to resolve sources shallower than 5 km from the observation plane. Although not displayed here, we also computed Euler solutions using a smaller window (3×3 grid cells), which did locate shallow solutions for SI=1. This indicates the presence of shallower dyke/sill sources within MLS, but as discussed above, we believe that these Euler depth estimates are unreliable due to the coarse grid cell spacing.

4.2. Magnetic anomalies, subglacial topography and ice flow

In Fig. 2c we overlay the Euler deconvolution solutions for SI=0 onto the bedrock topography derived from RES data. Our aim is to compare the location of possible geological contacts or large-throw faults with the subglacial topography. Bed elevation exhibits two significant highland blocks, which are labelled HB1 and HB2. HB1 is an elongated ENE–WSW oriented block, where most bed elevations are greater than 400 m. HB2 is a smaller, discrete subglacial mountain block. Four major topographic troughs are labelled T1–T4. The ENE–WSW section of L1 lies roughly parallel to the flank of trough T1, but is shifted southwards and lies within subglacial mountain block HB1. The WNW–ESE lineament L2 cuts across troughs T2 and T4, and appears to lie beneath subglacial highland HB2. The N–S oriented segments of L3 lie oblique to trough T1–T3, and to subglacial block HB1. Magnetic lineament L4 appears to coincide with the southern edge of trough T3.

In Fig. 2d, the same Euler solutions are overlain onto the velocity field as derived from combined InSAR and

balance velocities, to address the relationship between the location of magnetic lineaments and enhanced flow tributaries of Slessor Glacier. The three tributaries labelled STN, STC and STS lie approximately within subglacial troughs T1, T2 and T3, respectively. The tributaries are separated by two inter-tributary regions of low ice velocity labelled IT1 and IT2. Magnetic lineaments L1 and L4 appear to lie roughly parallel to the margins of tributaries STN and STS, respectively, but only L4 coincides with the tributary margin, as indicated along tie line T1020 by the intersection with a RAMP shear margin. In contrast, lineaments L2 and L3 run oblique to the tributaries. While L3 cuts across all three tributaries, L2 only crosses STC and terminates abruptly at the margin of IT2.

In Fig. 3 we compare aeromagnetic signatures along tie line T1020 with the location and velocities of the three tributaries of the Slessor Glacier. This profile view allows us to directly observe the high-frequency magnetic anomalies and hence address the shallow geological features beneath tributary and inter-tributary regions. The RAMP shear margins coincide with steep gradients in the velocity profile (Fig. 3a). The margins are hence used in the other panels to divide profiles into tributary and inter-tributary regions. As previously noted the tributaries lie in topographic troughs. In profile view (Fig. 3b) it becomes evident that trough T1, which underlies STN, is significantly deeper (1.27 km below sea level) than T2 and T3 (0.52 and 0.81 km, respectively). In contrast, magnetic anomalies are at a higher regional level over MLN compared to MLS (Fig. 3c). This suggests that the deeper geology beneath MLN and MLS may be different. The high-frequency pattern in the draped TMI also appears to differ between MLN and MLS, having less short wavelength features over MLN. This is enhanced in the residual produced by subtraction of the upward-continued (1 km) profile from the draped TMI (Fig. 3d). This suggests that there may also be a contrast in the shallow geological features beneath MLN and MLS. Further enhancement is seen in the residual calculated by subtraction of low-pass filtered data (Fig. 3e), which exhibits an abrupt discontinuity, coinciding roughly with the shear margin of STN. A near-zero amplitude of residual (AOR) is sustained over a 55 km wide area beneath STN. This "plateau" in AOR provides evidence for low susceptibility rock at the bed of subglacial trough T1. In contrast, no such "plateau" can be defined beneath T2 or T3, indicating that more highly magnetic rock units may underlie these troughs.

The AOR behaviour is not an artefact of varying topography. This is apparent from the agreement between profiles with and without draping (Fig. 3e). Draping only has a slight effect on the amplitudes in Fig. 3e. For example, above the subglacial highland block HB1, amplitudes are reduced after draping, correcting for bedrock which is closer to the aircraft. However, the AOR "plateau" over T1 is invariant to draping. Fig. 3(f) reveals that beneath the "plateau", no Werner solutions are located at depths shallower than 3 km below bedrock elevation. This is consistent with the inference made from the AOR, that relatively low susceptibility rock forms the bed of subglacial trough T1. Fewer solutions are expected beneath the "plateau", as higher amplitude short wavelength anomalies are required for a Werner solution. The method also provides us with an estimate of the depth to magnetic basement, which is approximately 3 km below bedrock. This depth estimate would be consistent with estimates independently derived from the slope of the radially averaged power spectrum (not shown) [17]. These results can be combined to place a lower bound on the thickness of low susceptibility rock beneath T1. Our Werner deconvolution results imply that outside T1, all susceptibility values were above 4×10^{-3} SI units, which is greater than typical sedimentary rock samples [18,19].

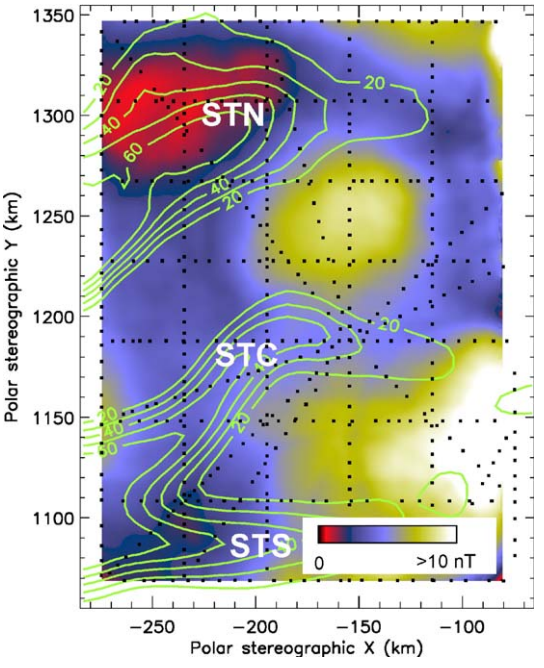

Fig. 4. Gridded AOR, providing a regional perspective of the variation in shallow magnetic susceptibility. Slessor Glacier tributary locations are indicated by velocity contours. Black dots represent the AOR peaks along the flight lines. Note that the inferred sedimentary basin beneath the northern tributary of the Slessor Glacier (STN), features AOR values close to 0.

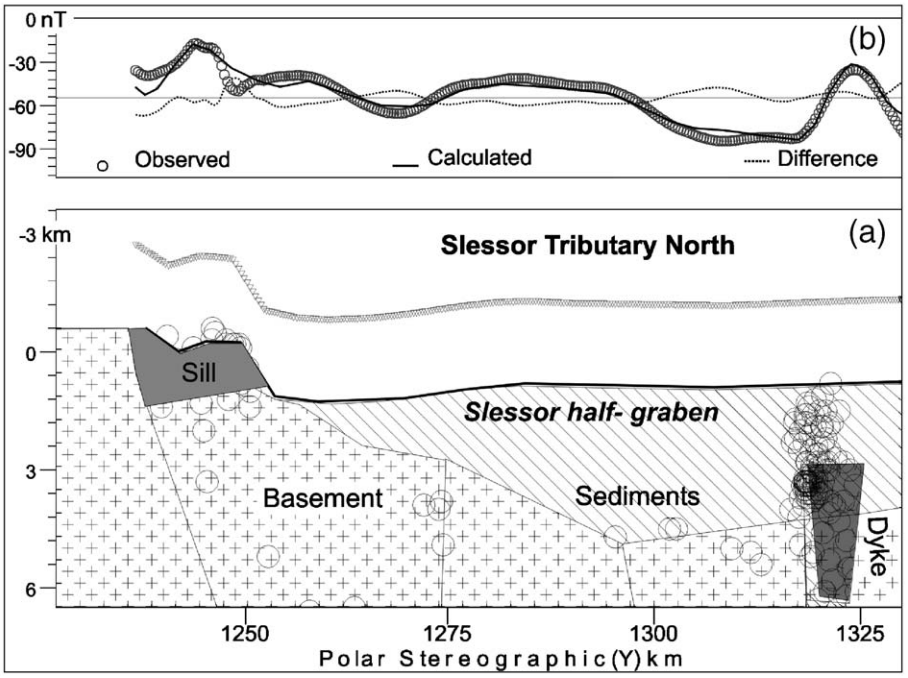

Fig. 5. Forward modelling across Slessor tributary north (see Fig. 2 for location) The circles represent 2D Werner deconvolution solutions. Flying altitude is shown by the grey triangles above the surface in (a). Apparent susceptibilities are between 5–12 10^{-3} SI units for the basement rock (crosses) and 15–20 10^{-3} SI units for the Jurassic sill and dyke complexes (grey). The diagonal hatched area shows the non-magnetic sedimentary infill of the Slessor half-graben structure interpreted as underlying STN. Werner solutions (circles) are at depths greater than 3 km below bedrock beneath this inferred sedimentary basin. The r.m.s error for this forward model is 6 nT.

Visual inspection of all flight lines that cross one or more tributary margins showed correlation between quiet sections of AOR and the presence of streaming ice, particularly beneath STN. To show this we built up a regional view of AOR in the whole survey area. By taking the values at localised peaks in all residual profiles, we gathered an irregular 2D distribution of AOR. These values, ranging from 0 to 40 nT, were then used to create a regular grid of 1 km cell spacing, by interpolation using a polynomial regression of power 2. Fig. 4 shows the resulting grid after a 9×9 cell boxcar smoothing to remove artefacts of the gridding algorithm.

4.3. Sedimentary basin beneath Slessor tributary north

The regional distribution of AOR in Fig. 4 implies a large (100×75 km) area of near-zero apparent susceptibility beneath STN. We suggest that this area defines the extent of a subglacial sedimentary basin beneath STN. To test this hypothesis we constructed a simple 2D forward model of the magnetic anomalies along the northern section of tie line T1020 (Fig. 5). Our model aims to assess if the estimates based upon Werner deconvolution of a 3 km thick sedimentary basin beneath STN may reproduce the observed magnetic anomaly patterns. The model was initially constructed by introducing a magnetic body within non-magnetic background. In order to fit the slope in the regional anomaly trend from higher values in the south to lower values in the north a dipping magnetic basement was necessary. Using values of apparent susceptibility of approximately 10×10^{-3} SI units and assuming a thickness of approximately 8 km the top of the dipping magnetic basement was found to lie at a depth of approximately 3 km below bedrock in the centre of STN. This is consistent with the independent Werner deconvolution depth estimates (Fig. 5). To fit the higher-frequency anomalies along the model profile, the magnetic block can be further split into 3 sub-blocks. A possible mesa is detected at the southern edge of the model profile and appears to be marked by a 60 nT high-frequency anomaly. The discrete anomaly peak at the northern edge of the profile required the introduction of an additional body with an apparent susceptibility of 22×10^{-3} SI units. Both the mesa and the dyke-like body are marked by roughly coincident Werner deconvolution clusters.

5. Discussion

5.1. Regional geological setting

A simple structural elements map was compiled from aeromagnetic data analyses over the Slessor Glacier tributaries and inter-tributary regions and forms the basis for our discussion (Fig. 6). To discuss the regional geological setting in the Slessor Glacier tributaries area we also inspected magnetic anomaly signatures previously detected over the Shackleton Range and the Theron Mountains (Fig. 1) [20,21],

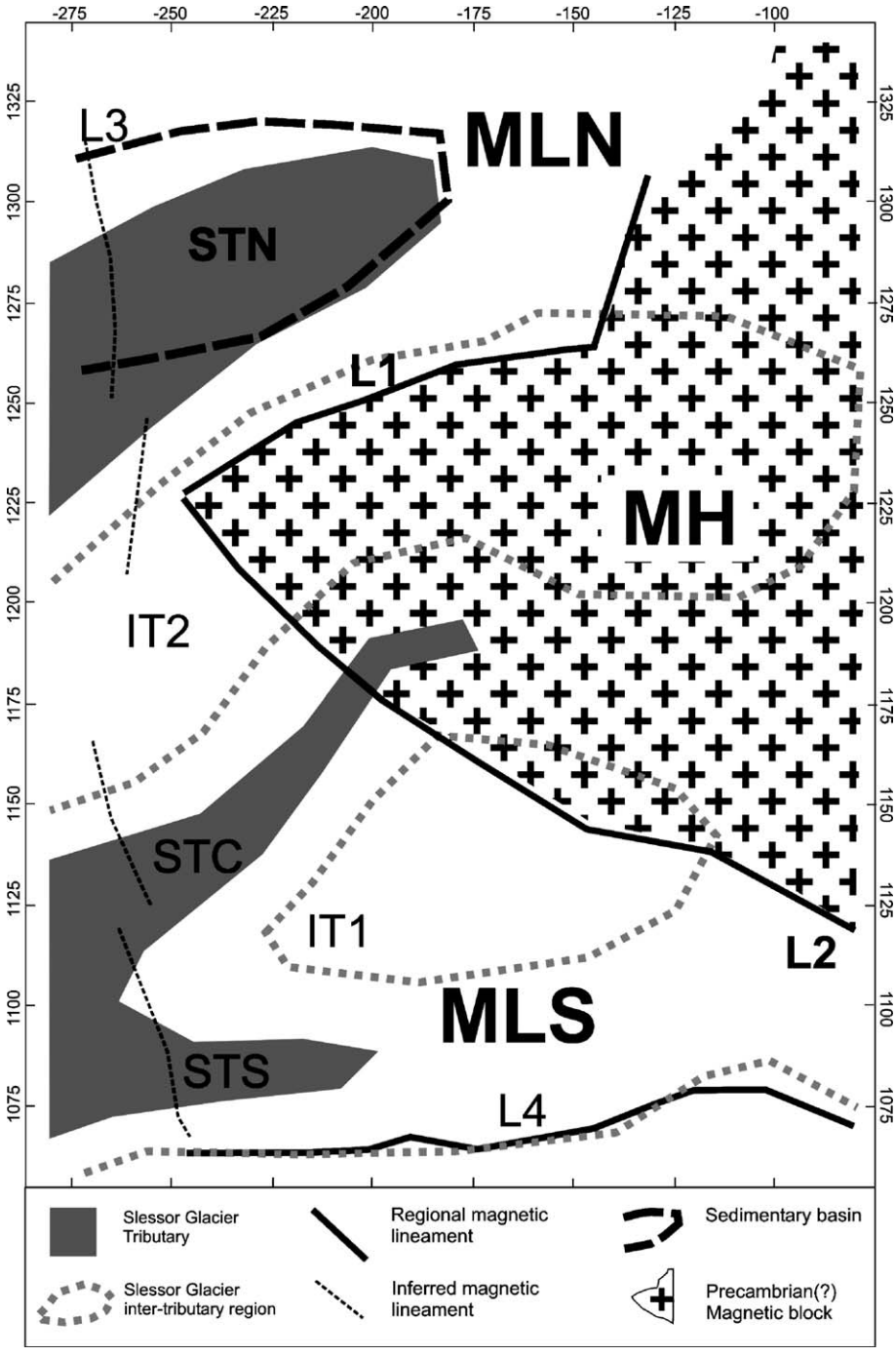

Fig. 6. Geological features and glaciological flow units over the Slessor Glacier as inferred from combined aeromagnetic and radio echo sounding data.

where geological investigations are fairly extensive [22].

The broad magnetic high, which dominates the eastern part of the survey area (MH), is interpreted as revealing Precambrian basement, perhaps composed of gneiss rock units. The area of enhanced ice flow lies adjacent to the proposed Precambrian block (Fig. 6). Sharp lineaments define the edges of the Precambrian block and are assumed to represent major faults. Interestingly, the trend of aeromagnetic lineaments L1 and L4 lies parallel to major thrust–faults of the Shackleton Range [23]. It is possible then, that these thrust faults, which lie parallel to Slessor Glacier and to Recovery Glacier in the Shackleton Range area, continue in our survey area, providing deep structural control over the location of the Slessor Glacier tributaries. However, some of the aeromagnetic lineaments, namely L2 and L3, lie highly oblique to the Slessor Glacier tributaries. These N–S to NNW trends are however sub-parallel to the transverse faults cutting the thrust faults of the Shackelton Range (Fig. 1 in [23]).

The Shackleton Range is a fault-bounded basement high, flanked by Beacon cover sedimentary rocks of the Whichaway Nunataks to the south and to the north by those of the Theron Mountains [24]. Beacon sedimentary rocks are intruded by Ferrar Jurassic sills and dykes in these regions. We suggest a similar geological setting in our study area. The Precambrian basement horst (MH) is bounded by two magnetic minima. The southern minima (MLS) features high-frequency magnetic anomalies (Fig. 3e), which we interpret as Jurassic Ferrar sills and dykes, intruding Beacon sediment. Similar high-frequency magnetic anomalies have been previously recognised in aeromagnetic profiles over the Theron Mountains [20], and have been attributed to the high magnetic susceptibilities of the Jurassic dolerites [25]. Our interpretation that high-frequency magnetic anomalies over Coats Land are caused by Ferrar rocks would also be consistent with extensive magnetic imaging of Ferrar dolerites over the Transantarctic Mountains and its ice-covered hinterland [14,26,27]. The magnetic quiet region over STN lacks these anomalies and is marked by the "plateau" in the AOR (Figs. 3e and 4). We suggest that this reflects an approximately 3 km thick (Fig. 3f) layer of post-Jurassic sedimentary rocks emplaced within a structurally controlled basin. Our 2D magnetic model (Fig. 5) suggests that a half-graben-like block underlies the northern tributary of the Slessor Glacier, and is flanked by Jurassic rocks on both sides. In particular the mesa subglacial topography on the southern flank of the basin is marked by a coincident high-frequency anomaly, as typically observed where Beacon sediments are intruded by Ferrar sills [14,26]. The northern flank of the basin appears to lack similar topography and the anomaly there may be related to dykes (Fig. 5). Our suggestion that a major post-Jurassic fault may flank a graben-like feature underlying the northern tributary of the Slessor Glacier, would be consistent with geological interpretations over the Shackleton Range [24].

5.2. Geological controls on ice flow

Three different geological controls on enhanced ice flow systems have been previously proposed, based upon interpretation of aerogeophysical data collected over the West Antarctic ice streams: 1) high-heat flow, associated with active, or recently active volcanism [28]; 2) sedimentary infill within narrow fault-bounded rift basins, [1] and 3) broader areas of marine sediment drape, deposited within the extended low-lying crust of the West Antarctic Rift system [3]. Of these three geological templates, high-heat flow associated with active volcanism is the least applicable to the Slessor Glacier tributaries. Our magnetic anomaly maps do not image the typical high-amplitude magnetic anomalies (up to 1000 nT) associated with late-Cenozoic volcanics in the West Antarctic Rift System [29,30]. In contrast, we suggest that the Slessor Glacier tributaries flank an old Precambrian block (Fig. 6), which is more likely to feature low regional heat flow compared to a Cenozoic rift system. In addition, there is no geological evidence in the adjacent Shackleton Range or in Theron Mountains for Cenozoic volcanism [22].

Narrow fault-bounded glaciated rift basins are best identified using airborne gravity data. Free-air and Bouguer gravity lows are typically observed over rift valleys due to topography and to the density contrast between sedimentary basin infill and adjacent basement rocks (e.g. [3]). No aerogravity data are currently available over the Slessor Glacier tributaries to validate or negate a rift hypothesis for subglacial basin T1, underlying STN. However, our aeromagnetic data suggest that in contrast to the situation observed over ice stream C in West Antarctica [1], the fault which appears to flank T1, may lie within the subglacial highland block (Fig. 2c), rather than directly along the margins of the ice stream.

The distinct "plateau" in the AOR, Werner deconvolution depth estimates, and our forward model all indicate the possibility of sedimentary infill within a structurally controlled basin beneath T1. After isostatic

adjustment, and taking into account raised sea levels in the past [31], we estimate that parts of T1 would have been submerged during ice free periods. Hence, this trough could potentially contain marine sediments deposited either prior to the formation of the East Antarctic Ice Sheet, or perhaps during a more recent deglaciation of East Antarctica during warm periods in the Neogene [32,33]. Estimates of basal roughness, derived from the RES bed returns, indicate a particularly smooth ice/bed interface in T1, in contrast to higher roughness in the inter-tributary regions and other troughs [34]. This would be compatible with the presence of a soft, deformable basal layer and/or with subglacial erosion via basal sliding [34]. In contrast, the central and southern tributaries of Slessor Glacier retain high-frequency magnetic anomalies, suggesting that any layer of post-Jurassic marine sediments within these troughs is relatively thin or has been eroded, and hence may not provide a first-order control on enhanced flow.

6. Conclusions

Data from airborne radio echo sounding and aeromagnetics have been combined to provide an inferred picture of the subglacial geology and its relation to ice flow for a region covering the three tributaries of Slessor Glacier, a major East Antarctic outlet glacier [35]. The main subglacial geological units we infer include a Precambrian block, Jurassic dykes and sills, and a post-Jurassic(?) sedimentary basin. The first two geological units show no clear relationship with subglacial topography, which appears to have a strong controlling influence on the location of the glacier tributaries. Several magnetic lineaments, interpreted as faults, lie oblique to the topographic troughs containing the tributaries. The exception to this, however, is the northernmost tributary, which was previously identified as having a significant portion of its motion taking place through basal sliding and/or a deforming layer of sediment [2]. Forward and inverse modelling of the magnetic anomaly data suggests the presence of a 3 km thick post-Jurassic(?) sedimentary basin beneath this tributary. The thickness of the sedimentary layer, combined with the depth of the trough suggests that the sediment is likely to be marine in origin. The new aeromagnetic evidence for a sedimentary basin beneath the northern tributary of the Slessor Glacier shows that subglacial sediments are potentially an important geological factor for controlling enhanced flow, not just for the WAIS [3], but also for the substantially larger EAIS.

Acknowledgements

This work was funded by UK NERC grant GR3/AFI2/65. We thank Ian Joughin for providing the InSAR-derived velocity data used here. Fieldwork in Antarctica was made possible by the British Antarctic Survey (BAS). Hugh Corr is acknowledged for his assistance with the aerogeophysical survey. In the field, we are particularly grateful to David Leatherdale, Phil Jones and Paul Woodroffe.

References

[1] R.E. Bell, D.D. Blankenship, C.A. Finn, D.L. Morse, T.A. Scambos, J.M. Brozena, S.M. Hodge, Influence of subglacial geology on the onset of a West Antarctic ice stream from aerogeophysical observations, Nature 394 (6688) (1998) 58–62.
[2] D.M. Rippin, J.L. Bamber, M.J. Seigert, D.G. Vaughan, H.F.J. Corr, Basal topography and ice flow in the Bailey/Slessor region of East Antarctica, J. Geophys. Res. 108 (F1) (2003).
[3] M. Studinger, R.E. Bell, D.D. Blankenship, C.A. Finn, R.A. Arko, D.L. Morse, I. Joughin, Subglacial sediments: a regional geological template for ice flow in West Antarctica, Geophys. Res. Lett. 28 (18) (2001) 3493–3496.
[4] F. Ferraccioli, M. Gambetta, E. Bozzo, Microlevelling procedures applied to regional aeromagnetic data: an example from the Transantarctic Mountains (Antarctica), Geophys. Prospect. 46 (2) (1998) 177–196.
[5] I. Joughin, L. Padman, Melting and freezing beneath Filchner-Ronne Ice Shelf, Antarctica, Geophys. Res. Lett. 30 (9) (2003) (art. no.–1477).
[6] I. Joughin, J.L. Bamber, Thickening of the ice stream catchments feeding the Filchner-Ronne Ice Shelf, Antarctica, Geophys. Res. Lett. 32 (2005) L17503, doi:10.1029/2005GL023844.
[7] J.L. Bamber, D.G. Vaughan, I. Joughin, Widespread complex flow in the interior of the Antarctic ice sheet, Science 287 (5456) (2000) 1248–1250.
[8] A.B. Reid, J.M. Allsop, H. Granser, A.J. Millett, I.W. Somerton, Magnetic interpretation in 3 dimensions using Euler deconvolution, Geophysics 55 (1) (1990) 80–91.
[9] L.L. Nettleton, Gravity and Magnetics in Oil Prospecting, McGraw-Hill, 1976.
[10] R.J. Blakely, Potential Theory in Gravity and Magnetic Applications, Cambridge University Press, 1995.
[11] M. Pilkington, J.B. Thurston, Draping corrections for aeromagnetic data: line- versus grid-based approaches, Explor. Geophys. 32 (2001) 95–101.
[12] R. Henderson, On the validity of the use of upward continuation integral for total magnetic intensity data, Geophysics 35 (5) (1970) 916–919.
[13] C.C. Ku, J.A. Sharp, Werner deconvolution for automated magnetic interpretation and its refinement using Marquardt inverse modeling, Geophysics 48 (6) (1983) 754–774.
[14] M. Studinger, R.E. Bell, W.R. Buck, G.D. Karner, D.D. Blankenship, Sub-ice geology inland of the Transantarctic Mountains in light of new aerogeophysical data, Earth Planet. Sci. Lett. 220 (3–4) (2004) 391–408.
[15] F. Alrawi, M. Brooks, A deep crustal model to explain regional aeromagnetic and gravity-anomalies in southwest England, Tectonophysics 212 (1–2) (1992) 109–115.

[16] E. Bozzo, A. Meloni, Geomagnetic anomaly maps of central Victoria Land (East Antarctica) from ground measurements, Tectonophysics 212 (1–2) (1992) 99–108.
[17] A. Spector, F.S. Grant, Statistical models for interpreting aeromagnetic data, Geophysics 35 (2) (1970) 293.
[18] M.B. Sergeyev, U.F. Meyer, A. Eckstaller, V.M. Mikhailov, The geological nature of the Haskard-Fuchs magnetic anomaly and identification of highly-magnetic rock units in the Shackleton Range, Antarctica, Terra Antartica 6 (3) (1999) 327–336.
[19] R.S. Carmichael, Practical Handbook of Physical Properties of Rocks and Minerals, CRC Press, 1990.
[20] A.V. Golynski, N.D. Aleshkova, Regional magnetic anomalies of the Weddell Sea region and their geological significance, Polarforforschung 67 (3) (2000) 101–117.
[21] A.V. Golynski, T. Morris, L.C. Kovacs, J.K. Ferris, A new magnetic map of the Weddell Sea and the Antarctic Peninsula, Tectonophysics 347 (2002) 3–11.
[22] S. Tessensohn, M.R.A. Thomson, The Euroshack project: a brief outline, Terra Antartica 6 (3) (1999) 175–182.
[23] W. Buggisch, G. Kleinshmidt, New evidence for nappe tectonics in the Southern Shackleton Range, Antarctica, Terra Antartica 6 (3) (1999) 203–210.
[24] S. Tessensohn, G. Kleinschmidt, W. Buggisch, Permo-carboniferous glacial beds in the Shackleton Range, Terra Antartica 6 (3) (1999) 337–344.
[25] M.B. Sergeyev, Magnetic properties of rocks from the south eastern part of the Weddell Sea region, Antarctica, Polarforforschung 67 (3) (2000) 119–124.
[26] F. Ferraccioli, E. Bozzo, Inherited crustal features and tectonic blocks of the Transantarctic Mountains: an aeromagnetic perspective (Victoria Land, Antarctica), J. Geophys. Res.-Solid Earth 104 (B11) (1990) 25297–25319.
[27] F. Ferraccioli, F. Coren, E. Bozzo, C. Zanolla, S. Gandolfi, I. Tabacco, M. Frezzotti, Rifted(?) crust at the East Antarctic Craton margin: gravity and magnetic interpretation along a traverse across the Wilkes subglacial basin region, Earth Planet. Sci. Lett. 192 (3) (2001) 407–421.
[28] D. Blankenship, R.E. Bell, S.M. Hodge, J.M. Brozena, J.C. Behrendt, C.A. Finn, Active volcanism beneath the West Antarctic ice sheet and implications for ice-sheet stability, Nature 361 (1993) 526–529.
[29] J.C. Behrendt, R. Saltus, D. Damaske, A. McCafferty, C.A. Finn, D. Blankenship, R.E. Bell, Patterns of late Cenozoic volcanic and tectonic activity in the West Antarctic rift system revealed by aeromagnetic surveys, Tectonics 15 (3) (1996) 660–676.
[30] J. Behrendt, Crustal and lithospheric structure of the West Antarctic Rift System from geophysical investigations — a review, Glob. Planet. Change 23 (1999) 25–44.
[31] T.J. Hughes, Ice Sheets, Oxford University Press, New York, 1998 343 pp.
[32] G.S. Wilson, J.A. Barron, A.C. Ashworth, R.A. Askin, J.A. Carter, M.G. Curren, D.H. Dalhuisen, E.I. Friedmann, D.G. Fyodorov-Davidov, D.A. Gilichinsky, M.A. Harper, D.M. Harwood, J.F. Hiemstra, T.R. Janecek, K.J. Licht, V.E. Ostroumov, R.D. Powell, E.M. Rivkina, S.A. Rose, A.P. Stroeven, P. Stroeven, J.J.M. van der Meer, M.C. Wizevich, The Mount Feather Diamicton of the Sirius Group: an accumulation of indicators of Neogene Antarctic glacial and climatic history, Palaeogeogr. Palaeoclimatol. Palaeoecol. 182 (1–2) (2002) 117–131.
[33] M.J. Hambrey, B. McKelvey, Major Neogene fluctuations of the East Antarctic ice sheet: stratigraphic evidence from the Lambert Glacier region, Geology 28 (10) (2000) 887–890.
[34] D.M. Rippin, J.L. Bamber, M.J. Seigert, D.G. Vaughan, H.F.J. Corr, The role of ice thickness and bed properties on the dynamics of enhanced flow tributaries of Bailey Ice Stream and Slessor Glacier, East Antarctica, Ann. Glaciol. 39 (2004) 366–372.
[35] D.G. Vaughan, J.L. Bamber, M. Giovinetto, J. Russell, A.P.R. Cooper, Reassessment of net surface mass balance in Antarctica, J. Climate 12 (4) (1999) 933–946.
[36] K.C. Jezek, H.G. Sohn, K.F. Noltimier, The radarsat Antarctic mapping project, in: Stein Ti (Ed.), 1998 International Geoscience and Remote Sensing Symposium (IGARSS 98) on Sensing and Managing the Environment, SEATTLE, WA, 6–10 Jul 1998, I E E E Service Center, 445 Hoes Lane, PO Box 1331, Piscataway, Nj 08855-1331, 1998, pp. 2462–2464.